CrossMark

Lanthanum phosphate/chitosan scaffolds enhance cytocompatibility and osteogenic efficiency via the Wnt/β-catenin pathway

Haoran Hu[1†], Peipei Zhao[2†], Jiayu Liu[2], Qinfei Ke[2], Changqing Zhang[1], Yaping Guo[2*] and Hao Ding[1*]

Abstract

Background: Fabrication of porous scaffolds with great biocompatibility and osteoinductivity to promote bone defect healing has attracted extensive attention.

Methods: In a previous study, novel lanthanum phosphate ($LaPO_4$)/chitosan (CS) scaffolds were prepared by distributing 40- to 60-nm $LaPO_4$ nanoparticles throughout plate-like CS films.

Results: Interconnected three dimensional (3D) macropores within the scaffolds increased the scaffold osteoconductivity, thereby promoting cell adhesion and bone tissue in-growth. The $LaPO_4$/CS scaffolds showed no obvious toxicity and accelerated bone generation in a rat cranial defect model. Notably, the element La in the scaffolds was found to promote osteogenic differentiation of bone marrow mesenchymal stem cells (BMSCs) through the Wnt/β-catenin signalling pathway and induced high expression of the osteogenesis-related genes alkaline phosphatase, osteocalcin and Collagen I (Col-I). Moreover, the $LaPO_4$/CS scaffolds enhanced bone regeneration and collagen fibre deposition in rat critical-sized calvarial defect sites.

Conclusion: The novel $LaPO_4$/CS scaffolds provide an admirable and promising platform for the repair of bone defects.

Keywords: Lanthanum, Nanoparticle, Bone defect, Osteogenesis, Wnt/β-catenin pathway

Background

A substantial challenge remains in the treatment of bone defects caused by skeletal injury or bone disease [1–3]. Although autogenous bone grafts are recognized as the "gold standard", their clinical application is restricted because of certain shortcomings, such as limited availability, additional pain, donor-position morbidity and infection risk [4]. Alternatively, various bone repair materials, including beta-tricalcium phosphate (β-TCP), hydroxyapatite (HA), bioactive glass (BG) and CS, have been recently developed [5, 6]. These biomaterials exhibit admirable biocompatibility and bioconductivity, but their limited osteoinductivity cannot meet the demands of patients, especially those with osteoporosis and metabolic disorders [7]. Consequently, developing a novel and osteoinductive platform for bone regenerations is a high priority.

The cell response and bone regeneration capacities of bone scaffolds can be improved by loading scaffolds with osteogenic growth factors/therapeutic drugs or doping with bioactive elements [8–10]. The introduction of bone morphogenetic protein 2, parathyroid hormone, vascular endothelial growth factor, bone forming peptide 1, or platelet derived growth factor in bone scaffolds effectively stimulates the osteogenic process of BMSCs and the formation of new bone tissues [11, 12]; however, the high concentrations of the released growth factors may cause side effects in the human body [13]. Another

---

*Correspondence: ypguo@shnu.edu.cn; docding1st@163.com
†Haoran Hu and Peipei Zhao contributed equally to this work
[1] Department of Orthopedic Surgery, Shanghai Jiao Tong University Affiliated Sixth People's Hospital, Shanghai Jiao Tong University, Shanghai 200233, China
[2] The Education Ministry Key Lab of Resource Chemistry and Shanghai Key Laboratory of Rare Earth Functional Materials, Shanghai Normal University, Shanghai 200234, China

strategy is to incorporate bioactive elements in bone scaffolds to enhance cell proliferation, differentiation and bone regeneration [14–16]. Lanthanum (La), one of rare earth elements (REEs) found in the human body, participates in stem cell differentiation, tissue regeneration and metabolism [17]. La can delay vascular calcification for patients with hyperphosphataemic renal bone disease and shows positive phosphate binding effects in bone metabolism [18]. Osteoclast formation and function are attenuated by $LaCl_3$ via down-regulation of rankl-induced Nf-κb and Nfatc1 activities [19]. In addition, lanthanum-containing nanoparticles have been reported as X-ray-mediated agents for tumour therapy [20]. Among the La-based bioceramics, $LaPO_4$ nanoparticles have attracted special attention because of their intrinsic photoluminescence property, low toxicity and good drug delivery behaviour [21–23]. Up to now, $LaPO_4$ nanoparticles have been widely used as imaging agents, drug carriers, and biomarkers [24, 25]. To the best of our knowledge, $LaPO_4$-coordination scaffolds have rarely been reported as bone regeneration materials, and their role in osteogenesis remains unclear.

Human bone has a complex inorganic–organic porous architecture, in 3D connected macrochannels facilitate nutrition transference and vascular and bone tissue in-growth [26]. CS, a common polysaccharide that is non-toxic, naturally degrades and exhibits good biocompatibility, has been widely used for bone repair materials [16, 27, 28].

Inspired by the architecture of natural bones, a novel and promising $LaPO_4$/CS scaffold was constructed using a freeze-drying technique. This is the first report showing that $LaPO_4$ nanoparticles in $LaPO_4$/CS scaffolds rapidly promote the osteogenesis activity of BMSCs, and the underlying mechanism was attributed to Wnt/β-Catenin pathway activation (Scheme 1). A skull bone repair model in Sprague–Dawley (S–D) rats further demonstrated that the $LaPO_4$/CS scaffolds significantly accelerate new bone regeneration compared with β-TCP/CS scaffolds. These exciting findings present a promising strategy for design and fabrication of novel REE-based biomaterials for skeletal treatments.

Experimental section

Preparation of $LaPO_4$ nanoparticles

$LaPO_4$ nanoparticles were fabricated by a chemical precipitation method. In brief, 2.9877 g $La(NO_3)_3\cdot6H_2O$ and 0.9112 g $(NH_4)_2HPO_4$ was separately dispersed in
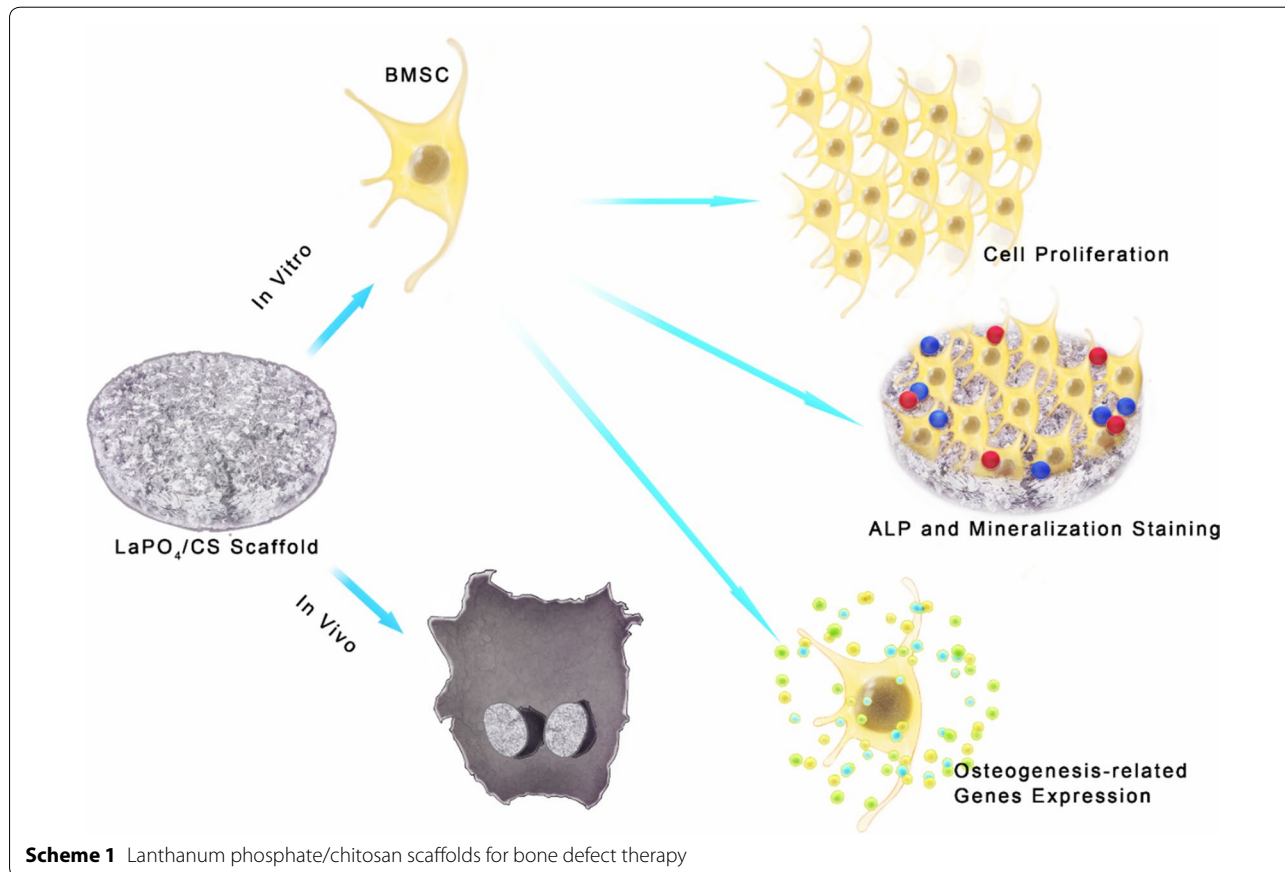
Scheme 1 Lanthanum phosphate/chitosan scaffolds for bone defect therapy

Hu *et al. J Nanobiotechnol*   (2018) 16:98

Page 3 of 13

100 mL deionized water. Then, the pH of an $(NH_4)_2HPO_4$ solution was adjusted to 11–12 by adding $NH_3·H_2O$ solution. The $La(NO_3)_3$ solution was dropwise dropped into the $(NH_4)_2HPO_4$ solution under continuous agitation at room temperature (RT). After 2.5 h, the mixture was stirred further for 1 h at 90 °C and then stirred for 24 h at RT. The precipitates were washed with deionized water and alcohol until the products were neutral. Finally, $LaPO_4$ nanoparticles were produced after drying at 60 °C for 24 h and calcination at 1000 °C for 3 h. Moreover, the β-TCP nanoparticles that served as the control group were prepared via a solid-state reaction [29, 30]. Calcium carbonate and ammonium phosphate (dibasic) mixtures at a molar ratio of 3:2 were calcined at 1000 °C for 3 h.

Preparation of LaPO₄/CS composite scaffold
Briefly, 4.0 g of CS powder was dissolved in 100 mL acetic acid solution (2.0 vol.%) to form a homogeneous CS solution. Then, 4.0 g of $LaPO_4$ was added into the CS solution, and the solution was stirred for 2 h. The mixture was injected into wells in 24-well or 96-well plates. The samples were frozen at −20 °C for 12 h and then freeze-dried in a freeze drier at −60 °C for 48 h. The as-obtained precursor scaffolds were dipped in 0.1 mol/l sodium hydroxide solution for 24 h, followed by washing with deionized water for 6 days. β-TCP/CS scaffolds were prepared by the same method.

Characterization
$LaPO_4$ nanoparticles and $LaPO_4$/CS scaffolds were coated with a thin gold layer, and then their morphologies were characterized by field-emission scanning electron microscopy (SEM; S-4800, Hitachi, Japan). The accelerating voltage was 5 kV and the working distance was kept at approximately 7 mm. The element compositions were determined by energy dispersive spectrometry (EDS; Quantax 400, Bruker) at an accelerating voltage of 20 kV. The microstructures of $LaPO_4$ nanoparticles were characterized by high resolution transmission electron microscopy (HRTEM; JEM-2100, JEOL, Japan) and selected area electron diffraction (SAED) at 200kv. The phases of the samples were characterized by X-ray powder diffraction (XRD; D/Max-2200, Rigaku, Japan) using Cu Kα radiation at 40 kV with a scanning speed of 5°/min in the range of $2\theta = 10°–70°$. The functional groups in samples were detected by Fourier transform infrared spectroscopy (FTIR; Frontier, PerkinElmer, USA) in a wavenumber range of 4000–500 cm^{-1} with a resolution of 4 cm^{-1} at 100~230 V. A Malvern Zetasizer (Nano ZS90; Malvern Instruments Ltd. UK) was employed for dynamic light scattering (DLS) measurements after the $LaPO_4$ particles were dispersed in ultrapure water. The organic and inorganic percentages

of the scaffolds were calculated according to thermogravimetric analysis (TG; Perkin-Elmer) with a heating rate of 10 °C/min. The as-used purge gas was dry air with a flow rate of 50 mL/min and a heating rate of 10 °C/min.

Cell isolation and culture
Rat bone marrow mesenchymal stem cells (BMSCs) were isolated from the femur of S–D rats using a Ficoll density gradient and then allowed to proliferate in minimum essential medium α (Gibco) with 10% foetal bovine serum (Gibco), penicillin (100 U/mL) and streptomycin (100 μg/mL) (Gibco) in an incubator with 5% CO_2 at 37 °C. The cells used in this study were from passages 3–7.

Cell morphology on scaffolds
To observe the attachment of cells on both $LaPO_4$/CS and β-TCP/CS scaffolds, BMSCs were cultured on the scaffolds at a density of 2.0×10^4 cells/mL in a 24-well plate. After 3 days of incubation, the cells were fixed with 2.5% glutaraldehyde, washed with phosphate buffer saline (PBS), dehydrated by ethanol, and freeze-dried at −80 °C. Finally, SEM (S-4800, Hitachi, Japan) was utilized to observe the samples.

Cell toxicity and proliferation on scaffolds
To estimate the cell toxicity and proliferation of the scaffold, on days 1, 3 and 7, Cell Counting Kit 8 (CCK-8; Dojindo, Japan) was adopted measure the cell viability. In brief, 1.0×10^4 BMSCs were co-cultured with scaffolds in a 24-well plate for the given days. At each time point, 450 μL of culture medium with 50 μL (10%) of CCK-8 reagent was added to the samples. The cells were incubated for 2 h, and then, the absorbance at 450 nm was measured with a microplate reader (Bio-Rad, USA).

Alkaline phosphatase (ALP) activity assay and staining
To carry out the ALP activity assay and staining, BMSCs were seeded on the $LaPO_4$/CS and β-TCP/CS scaffolds for 7 and 14 days in a 24-well transwell plate at a primary density of 2.0×10^4 cells/mL, with cells in the lower chamber and the scaffolds in the upper chamber. At each time point, the ALP activity was determined via the p-nitrophenyl-phosphate (pNPP) method, and ALP staining was conducted via the 5-bromo-4-chloro-3-indolyl phosphate/tetranitroblue tetrazolium chloride (BCIP/NBT) method according to the manufacturer's instructions. For the ALP activity assay, the samples were washed twice with PBS and lysed with 0.1% Triton X-100, and then pNPP (Beyotime Biotechnology, China) was added for 60 min at 37 °C. Last, 1 M NaOH solution was added to quench the chromogenic reaction, and the absorbance at 405 nm of each sample was recorded. For ALP staining, a BCIP/NBT kit (Beyotime Biotechnology,

Hu *et al. J Nanobiotechnol*   (2018) 16:98

Page 4 of 13

Table 1 Real-time polymerase chain reaction primers used in this study

Gene	Accession number	Primers (up: forward; down: reverse)	Product size (bp)
GAPDH	NM_017008.4	GCAAGAGAGAGGCCCTCAG TGTGAGGGAGATGCTCAGTG	74
OCN	NM_013414.1	TCACTCTGCTGGCCCTGACT CCCTCCTGCTTGGACATGAA	100
ALP	NM_013059.1	CATCATCATGTTCCTGGGAG GACCTGAGCGTTGGTGTTGT	163
Col-I	NM_053304.1	GGCGAGTGCTGTCCTTTCTG CTTCCCCATCATCTCCGTTCT CTTCC	434

China) was used to stain the samples, which were photographed with both a digital camera (Canon, Japan) and a microscope (Leica, Germany).

Extracellular matrix (ECM) mineralization evaluation

Cells were cultured in a 24-well transwell plate. After 7 and 14 days of culture, the cells were fixed with 2.5% glutaraldehyde and washed twice with PBS. The samples were stained with 1 mM alizarin red (Cyagen, USA) for 10 min. Finally, images were acquired with both a digital camera and a microscope.

Osteogenesis-related gene expression

Cells were seeded on the $LaPO_4$/CS and β-TCP/CS scaffolds at a density of 2.0×10^4 cells/mL in a 6-well plate for 7 and 14 days, and then, Trizol (Invitrogen) was used to extract messenger RNA (mRNA) from the cells, and Moloney Murine Leukemia Virus (M-MLV) Reverse Transcriptase (Takara) was used to synthesize the complementary DNA (cDNA). qPCRSuperMix (BioTNT), forward and reverse primers and cDNA were loaded onto a 384-well plate, and the reverse transcription-polymerase chain reaction (RT-PCR) procedure was performed using a Sequence Detection System (7900 HT, ABI). The primers used in this study are shown in Table 1, and GAPDH was used as the internal control gene.

Western blotting

The protein in rBMSCs from different groups was extracted with cell lysis buffer and proteinase inhibitor after 7 and 14 days of culture. A bicinchoninic acid Protein Assay Kit (Cell Signaling Technology) was used to quantify the protein concentrations. Each protein sample was loaded onto sodium dodecyl sulfate–polyacrylamide gel electrophoresis gels for electrophoresis (Millipore) and then transferred to polyvinylidene difluoride membranes. After blocking with Quickblock™ (Beyotime), the membrane was incubated with primary antibody targeting phosphorylated glycogen synthase kinase-3β (p-GSK3β), glycogen synthase kinase-3β (GSK3β), β-Catenin and GAPDH at 4 °C overnight and then with secondary antibodies at RT for 2 h.

Procedures for Implantation of the Scaffolds into Animals

All animal surgical procedures were approved by the Animal Care and Experiment Committee of Shanghai Jiao Tong University Affiliated Sixth People's Hospital. Twenty adult S–D rats (8 weeks old; weight 250 ± 25 g) were anaesthetized by intraperitoneal injection of chloral hydrate sodium (250 mg/kg). An incision with a sagittal length of 1.5–2.0 cm was made on the scalp, and then, two full-thickness 5-mm-diameter defects were made on both sides of the skull with an electric trephine drill. The scaffolds implanted were 5 mm in diameter and 2 mm in thickness and randomly implanted into each cranial defect. The rats were intraperitoneally injected with fluorochromes under anaesthesia as follows: 25 mg/kg tetracycline (Sigma, USA) on week 3, 30 mg/kg alizarin red (Sigma, USA) on week 6 and 20 mg/kg calcein (Sigma, USA) on week 9. On week 12, all rats were sacrificed by intraperitoneal injection with an overdose of hydrate sodium, and the calvarias were obtained.

Micro-CT and histomorphometric analyses

The skull specimens were scanned using micro-computerized tomography (micro-CT, Skyscan, Belgium). Scanning was performed with a 100 kV/100 µA X-ray source with an isotropic voxel size of 18 µm. The images were used to reconstruct tomograms with a 3D Creator software (Skyscan Software). Bone mineral density (BMD) and the ratio of bone volume/tissue volume (BV/TV) were measured with CTAn (Skyscan Software) based on the reconstructed micro-CT images.

Histological analysis

For histological analysis, the specimens were dehydrated in a graded alcohol series for 3 days and then embedded in methyl methacrylate without decalcification. The non-decalcified samples were cut with a diamond saw (SP1600, Leica) and ground to approximately 150 µm in thickness. After fluorescence labelling, the specimens were evaluated with a confocal laser scanning microscope (Leica). After Van Gieson's (VG) staining, the specimens were observed with an optical microscope (Leica).

Statistical analysis

Statistical analyses were performed using SPSS 20.0 (SPSS Inc., Chicago, IL, USA). All the data were expressed as mean ± standard deviation and analysed by one-way analysis of variance with Bonferroni's post hoc test. Statistical significance was indicated when $p < 0.05$.
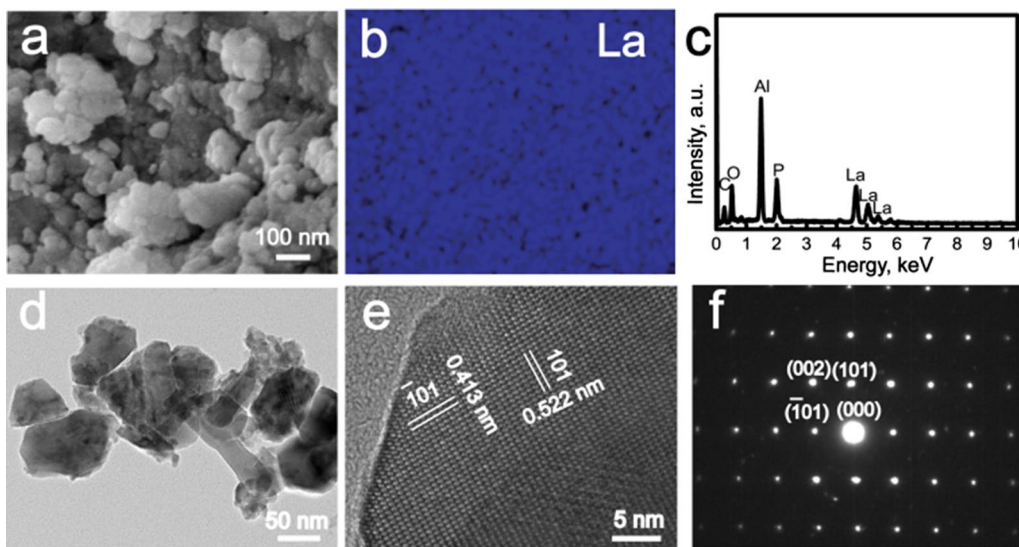
Hu *et al. J Nanobiotechnol*   (2018) 16:98

Page 5 of 13

Fig. 1 Characterization of LaPO$_4$ nanoparticles: **a** SEM image; **b** image showing La distribution; **c** EDS spectrum; **d** TEM image; **e** HRTEM image; **f** SAED pattern

Results

Morphologies and Structures of LaPO$_4$/CS Scaffolds

Inspired by the hierarchical architecture of bone, LaPO$_4$/CS scaffolds were constructed according to the following steps: (i) coprecipitation preparation of LaPO$_4$ nanoparticles; and (ii) freeze–drying synthesis of the LaPO$_4$/CS scaffolds. SEM and TEM images showed that the as-obtained LaPO$_4$ nanoparticles exhibited irregular shapes with sizes of approximately 40–60 nm (Fig. 1a, d). The nanostructure of LaPO$_4$ can increase the surface energy, easily resulting in the agglomeration of these nanoparticles (Fig. 1a). The hydrodynamic sizes of LaPO$_4$ agglomerates were mainly distributed at around 500 nm, as detected by a Malvern Zetasizer Nano ZS90 instrument (Additional file 1: Figure S1). As shown in the EDS spectrum (Fig. 1c), the elements La, P and O were present in the LaPO$_4$ nanoparticles, and Al was present in the aluminium foil. La was uniformly dispersed within the LaPO$_4$ nanoparticles (Fig. 1b). A representative HRTEM image taken from an individual LaPO$_4$ nanoparticle showed a lattice spacing of 4.138 Å and 5.227 Å, which can be indexed to the ($\bar{1}$01) and (101) crystal planes of LaPO$_4$, respectively (Fig. 1e). The SAED pattern the LaPO$_4$ nanoparticles exhibited bright spots, indicating a monocrystal structure with a [01$\bar{1}$] zone axis.
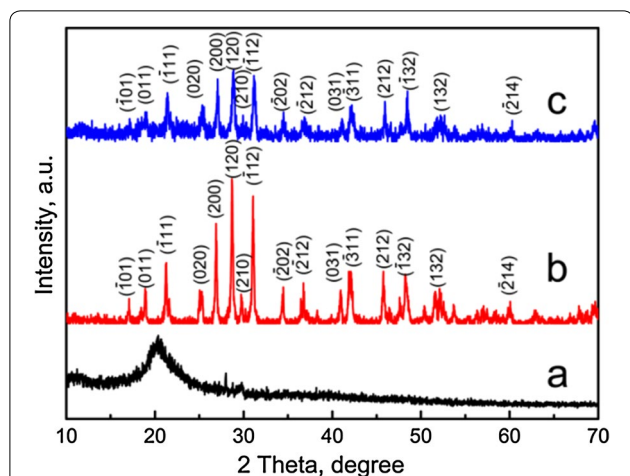

Fig. 2 XRD patterns of samples: **a** CS; **b** LaPO$_4$ particles; **c** LaPO$_4$/CS composite scaffold
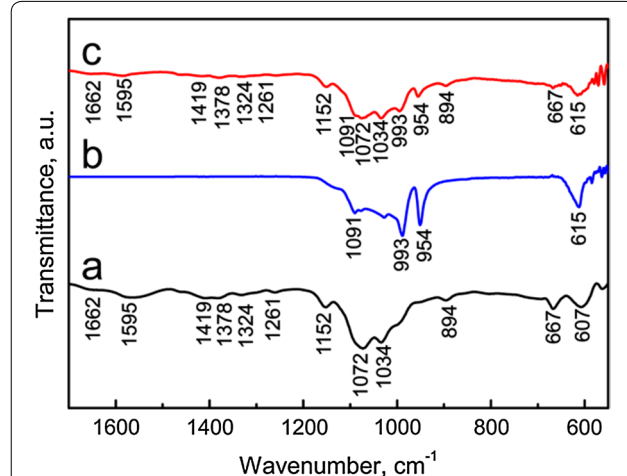

Fig. 3 FTIR spectra of samples: **a** CS; **b** LaPO$_4$ particles; **c** LaPO$_4$/CS composite scaffold

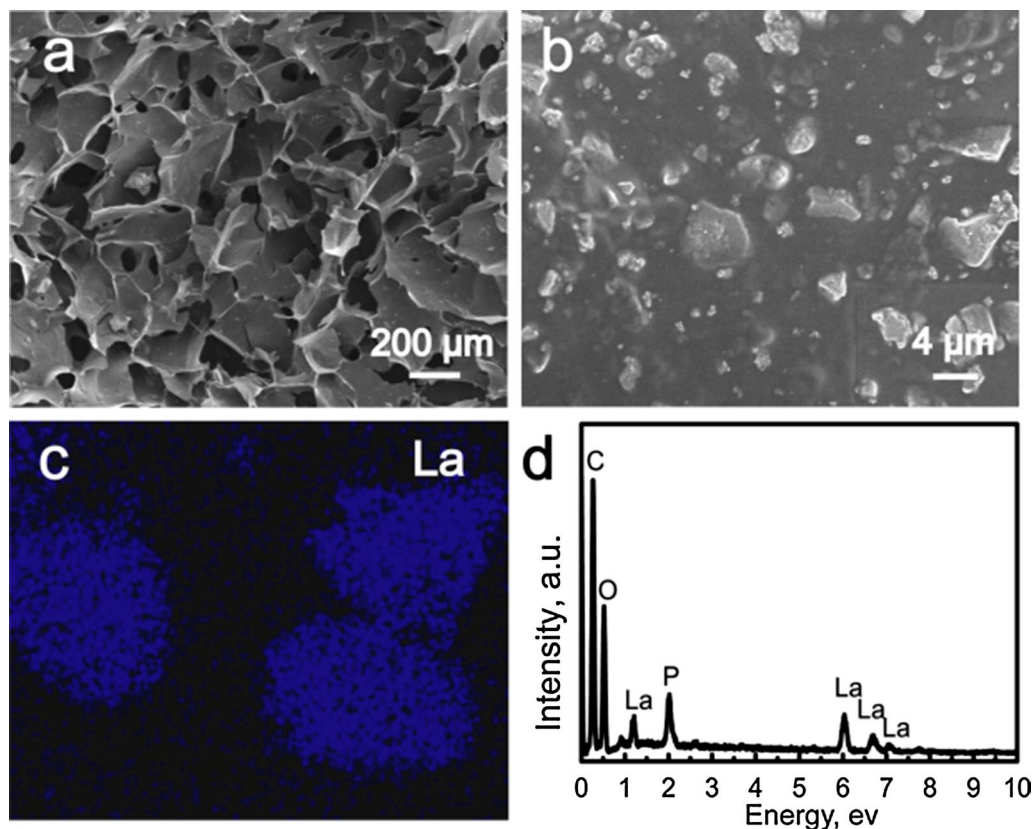Hu *et al. J Nanobiotechnol*   (2018) 16:98

Page 6 of 13

Fig. 4 Characterization of LaPO$_4$/CS scaffolds: **a**, **b** SEM images; **c** surface scan map of La; **d** EDS spectrum

The phases of the LaPO$_4$/CS scaffolds were investigated by XRD patterns using pure CS and LaPO$_4$ as control groups (Fig. 2). The characteristic peaks of LaPO$_4$ nanoparticles indicated a monoclinic phase with a space group of *P*21/*n*(14) (JCPDS 16-0382) [31]. As we know, the structure units of CS include β-(1,4)-2-acetamido-2-β-ᴅ-glucose and β-(1,4)-2-amido-2-β-ᴅ-glucose units [32]. The diffraction peaks at approximately 20° and 28° revealed that the pure CS exhibited semi-crystalline features (Fig. 2a). Compared with the pure CS and LaPO$_4$, only characteristic peaks of LaPO$_4$ were detected in the LaPO$_4$/CS scaffolds due to the lower crystallinity of CS relative to LaPO$_4$ (Fig. 2).

The functional groups of the LaPO$_4$/CS scaffolds were demonstrated by FTIR spectra using pure CS powders and LaPO$_4$ as control groups. The LaPO$_4$/CS scaffolds possessed the characteristic bands of both LaPO$_4$ and CS (Fig. 3). For the LaPO$_4$/CS scaffolds and CS powders (Fig. 3a, c), the bands at 1662, 1595 and 894 cm^{-1} corresponded to the amide-I vibration, N–H deformation vibration and N–H wagging vibration in amino groups, respectively [33]. The C-O stretching vibration bands were located at 1072/1034 cm^{-1}, and the bridge oxygen stretching vibration bands were located at 1152 cm^{-1} [34]. The characteristic bands of PO$_4^{3-}$ groups were observed in both the LaPO$_4$/CS scaffolds and LaPO$_4$ nanoparticles. The P-O antisymmetric stretching vibration (v_3) band was located at 993 and 954 cm^{-1}, and the antisymmetric deformation vibration (v_4) band was located at 615 cm^{-1} [35, 36].

The morphologies of LaPO$_4$/CS scaffolds were characterized by SEM, as shown in Fig. 4. The LaPO$_4$/CS scaffolds possessed 3D interconnected macrochannels with pore sizes of approximately 200 μm (Fig. 4a). These interlinked macropores, which were formed due to volatilization of ice crystals during the freeze-drying procedure, can promote body fluid exchange and bone tissue ingrowth [26]. The CS films were connected together, and the macropores were present among the films. Moreover, the LaPO$_4$ nanoparticles were distributed within or on the CS films, and they presented a granule-stacking structure because of their small particle sizes (Fig. 4b). A La surface scan map of La further demonstrated the presence of LaPO$_4$ nanoparticles within the scaffolds (Fig. 4c). The EDS spectrum indicated that the LaPO$_4$/CS composite scaffolds were composed of the elements La, P, O and

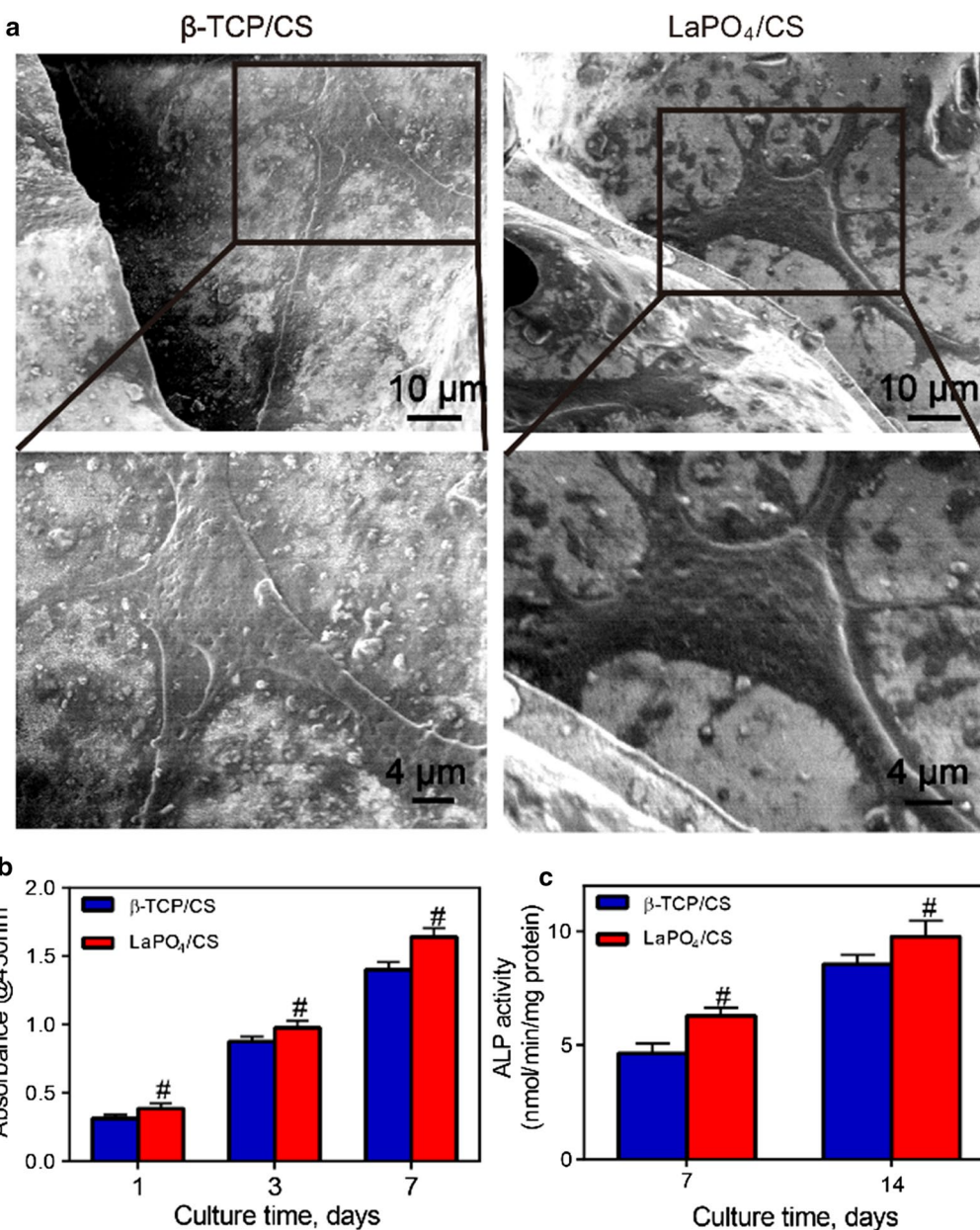Hu *et al. J Nanobiotechnol* (2018) 16:98

Page 7 of 13

Fig. 5 a SEM images of the LaPO$_4$/CS and β-TCP/CS scaffolds after 3 days of incubation with rBMSCs. **b** CCK-8 results on days 1, 3 and 7; **c** ALP activity results on days 7 and 14 (#: a significant difference compared with the β-TCP/CS group (*p < 0.05*))

C (Fig. 4d). The elements La and P were ascribed to the LaPO$_4$ nanoparticles, and C was ascribed to the CS. The TG curves indicated that the volatilization of adsorbed water took place at 40–100 °C, while the decomposition of CS occurred at 100–550 °C (Additional file 1: Figure S2). The percentages of different components in the scaffolds could be calculated according to the TG curves. The percentages of adsorption water, LaPO$_4$ and CS in the LaPO$_4$/CS scaffolds were approximately 9%, 47%

and 44%, respectively (Additional file 1: Figure S2a). The percentages of adsorption water, LaPO$_4$ and CS in the LaPO$_4$/CS scaffolds were approximately 7%, 47% and 46%, respectively (Additional file 1: Figure S2b).

In Vitro Cytocompatibility and Osteogenesis Ability of LaPO$_4$/CS Scaffolds

The cytocompatibility and osteogenesis ability of the LaPO$_4$/CS scaffolds were assessed using rBMSCs as the

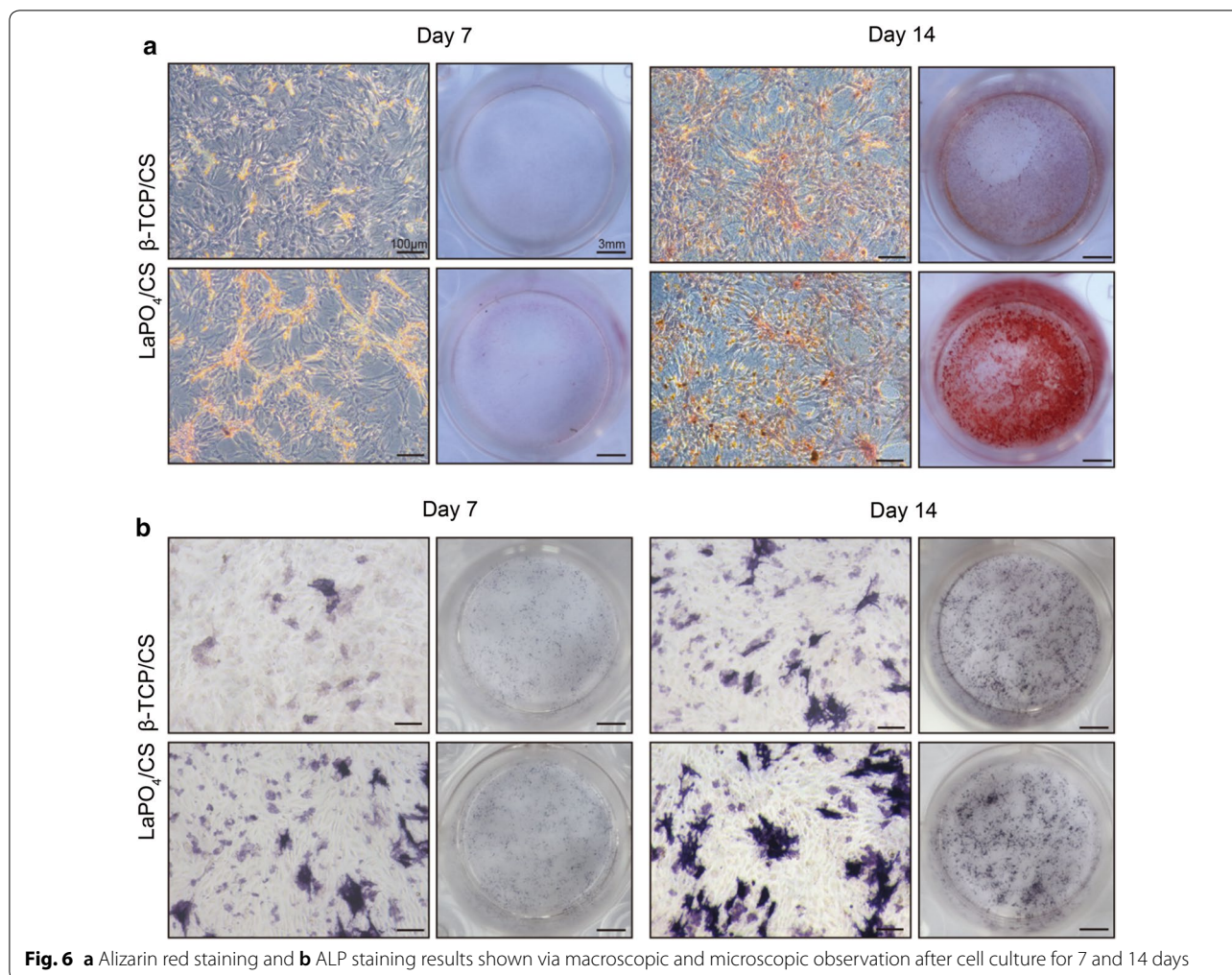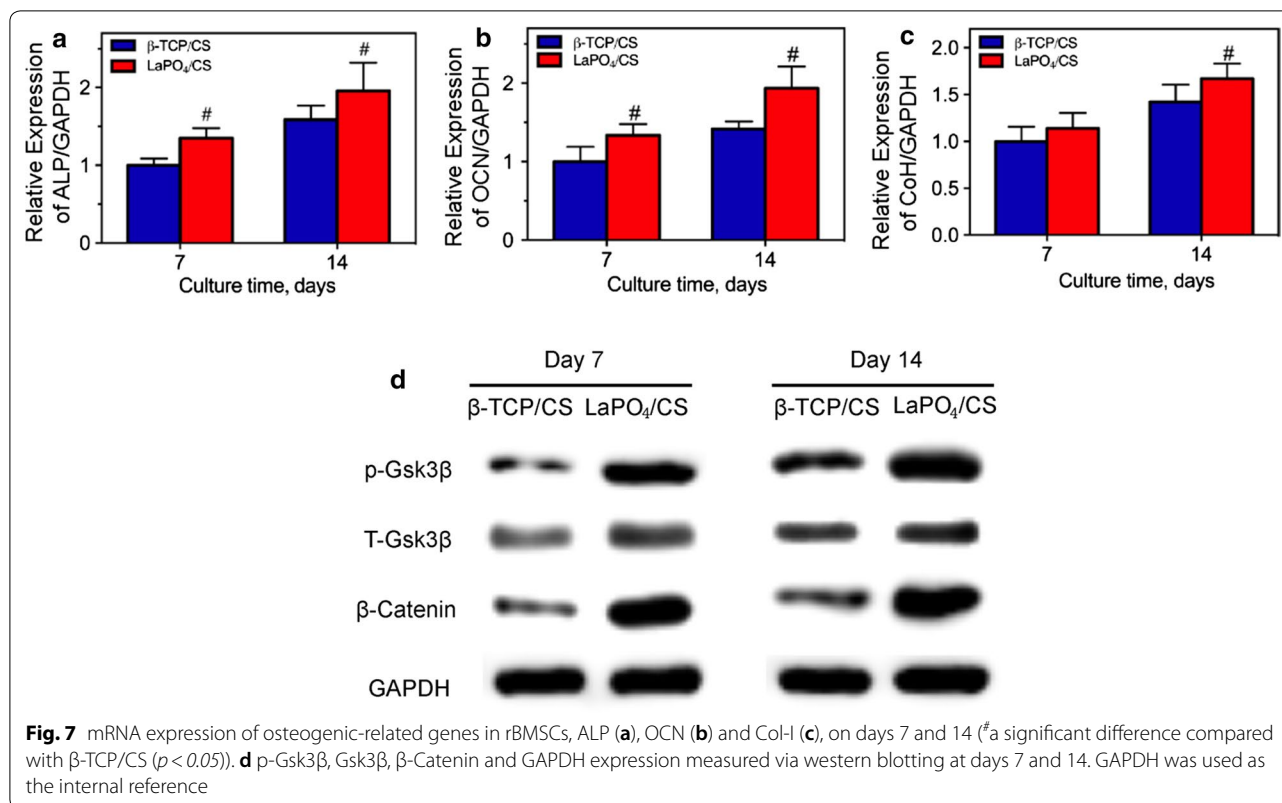Hu *et al. J Nanobiotechnol*   (2018) 16:98

Page 8 of 13

Fig. 6 a Alizarin red staining and **b** ALP staining results shown via macroscopic and microscopic observation after cell culture for 7 and 14 days

cell model and β-TCP/CS scaffolds as the control group. SEM images indicated that the rBMSCs attached tightly to the films of both the LaPO$_4$/CS scaffolds and β-TCP/CS scaffolds after 3 days of culture (Fig. 5a). Long cell pseudopodia spread well and stretched gradually into the scaffold interior through the interconnected macropore channels. The cells on both the LaPO$_4$/CS scaffolds and β-TCP/CS scaffolds continuously proliferated from day 1 to day 7, as shown by the CCK-8 results (Fig. 5b). Notably, the cell number on the LaPO$_4$/CS scaffolds was significantly greater than that on the β-TCP/CS scaffolds ($^{\#}p < 0.05$, Fig. 5b) after culture for 1, 3 or 7 days, suggesting that the LaPO$_4$/CS scaffolds remarkably supported the proliferation of rBMSCs compared with the β-TCP/CS scaffolds.

The osteogenesis ability of the LaPO$_4$/CS scaffolds was determined by ALP activity, ALP staining and mineralization evaluation assays. ALP activity is an early osteogenic differentiation marker secreted by stem cells. The ALP activity in the LaPO$_4$/CS group was significantly higher

than that in the β-TCP/CS group (Fig. 5c, $^{\#}p < 0.05$). ALP staining images further demonstrated that the cells co-cultured with the LaPO$_4$/CS scaffolds produced more ALP than those with cultured with the β-TCP/CS scaffolds at days 7 and 14 (Fig. 6b). Meanwhile, macroscopic and microscopic alizarin red staining images revealed that the rBMSCs in the LaPO$_4$/CS group generated more ECM mineralization than those in the β-TCP/CS group at days 7 and 14 (Fig. 6a). Taken together, the in vitro cell tests suggest that both the LaPO$_4$/CS and β-TCP/CS scaffolds present excellent cytocompatibility, and the LaPO$_4$/CS scaffolds exhibited better osteogenic effects than the β-TCP/CS scaffolds.

To further investigate the underlying osteogenesis mechanism of the LaPO$_4$/CS scaffolds, the expression of osteogenesis-related genes in the BMSCs co-cultured with the LaPO$_4$/CS and β-TCP/CS scaffolds was evaluated by RT-PCR and western blot analysis (Fig. 7). After culture for 7 or 14 days, the expression levels of ALP and osteocalcin (OCN) in the LaPO$_4$/CS group

Hu *et al. J Nanobiotechnol*   (2018) 16:98

Page 9 of 13

Fig. 7 mRNA expression of osteogenic-related genes in rBMSCs, ALP (**a**), OCN (**b**) and Col-I (**c**), on days 7 and 14 ([#]a significant difference compared with β-TCP/CS ($p < 0.05$)). **d** p-Gsk3β, Gsk3β, β-Catenin and GAPDH expression measured via western blotting at days 7 and 14. GAPDH was used as the internal reference

were significantly increased compared with those in the β-TCP/CS group (Fig. 7a, b). Although the expression level of Col-I showed no significant difference between the LaPO$_4$/CS and β-TCP/CS group at day 7, the Col-I expression level in the former was much greater than that in the latter at day 14 (Fig. 7c). Moreover, western blotting results revealed that the LaPO$_4$/CS scaffolds obviously enhanced the expression of phosphorylated Gsk3β and β-Catenin compared with the β-TCP/CS scaffolds (Fig. 7d). Gsk3β and β-Catenin are key proteins in the Wnt/β-catenin pathway. Therefore, it can be inferred that the LaPO$_4$/CS scaffolds enhance osteogenesis activity by activating the Wnt/β-catenin signalling way.

Bone regeneration ability in vivo

The in vivo bone formation capacity of the LaPO$_4$/CS scaffolds was evaluated using critical-sized calvarial bone defect models. 3D reconstructed micro-CT images indicated that the LaPO$_4$/CS scaffolds had a better ability to promote new bone formation in the cranial defects than the β-TCP/CS scaffolds after 12 weeks of implantation (Fig. 8a). Simultaneously, the calculated BMD and BV/TV values confirmed the above conclusion. The LaPO$_4$/CS group showed a higher BMD (0.577 ± 0.053) than the β-TCP/CS group (0.379 ± 0.037) (Fig. 8b, $p < 0.05$). The BV/TV ratio in the LaPO$_4$/CS scaffold group was also

increased up to $49.87 \pm 2.91\%$ compared with the β-TCP/CS group ($37.85 \pm 2.44\%$) (Fig. 8c, [#]$p < 0.05$).

The newly formed bone was characterized at different weeks post-operation via histological analysis of triple fluorescence labelling, specifically tetracycline (yellow) at week 3, calcein (green) at week 6 and alizarin red (red) at week 6 (Fig. 8d). Stronger density and a more widely spread area of fluorescence were detected in the LaPO$_4$/CS group than in the β-TCP/CS group. Moreover, VG staining (Fig. 9) suggested more collagen fibres were present surrounding the sites of the LaPO$_4$/CS scaffolds than surrounding the β-TCP/CS scaffolds, indicating that the LaPO$_4$/CS scaffolds exhibited better potential for collagenous matrix formation. Taken together, the micro-CT reconstruction, fluorescence labelling and VG staining results demonstrated that the LaPO$_4$/CS scaffolds could better enhance both in vivo new bone formation and collagen formation than the β-TCP/CS scaffolds.

Discussion

Developments in nanotechnology, molecular biology and nanomedicine have facilitated the fabrication of various biomedical materials [37, 38]. To date, a large number of bone repair materials have been developed for treating bone defects; however, their low bone-forming ability still cannot meet the demands of patients, especially

Hu *et al. J Nanobiotechnol*   (2018) 16:98

Page 10 of 13

those with osteoporosis and metabolic disorders [6]. Notably, REEs play a pivotal role in regulating the function and performance of bone tissues. Hence, here, novel LaPO$_4$/CS scaffolds were developed for the first time for use as bone repair materials.

Excellent osteoconductivity and biocompatibility are prerequisites for bone tissue engineering materials. It has been reported that CS has biological and chemical similarities to natural tissues, which could promote the proliferation of mesenchymal cells such as BMSCs and stimulate its differentiation [39, 40]. Combination of natural chitin-calcium-carbonate-protein complexes can result in hardening of the CS scaffold [41]. The 3D CS-based scaffolds were reported to provide a proper space for new bone tissue regeneration with optimal size of 200-600 μm to facilitate osteoconduction and bone growth [42]. During the freeze-drying process, a 3D interconnected macroporous structure with pore sizes of

Fig. 8 a Micro-CT results of 3D reconstructed and 2D sagittal images and the BMD (**b**) and BV/TV (**c**) results ($^#$a significant difference compared with β-TCP/CS, *p < 0.05*). **d** New bone formation and mineralization determined by fluorochrome-labelling analysis. Row 1 (yellow) shows tetracycline at week 2, row 2 (red) shows alizarin red at week 4, row 3 (green) shows calcein at week 6, and row 4 shows merged images of the three fluorochromes for the same group

approximately 200 μm was produced by using ice crystals as templates (Fig. 4). The large macropores not only provided enough spaces for cell adhesion and pseudopodium migration (Fig. 5a) but also supported the in-growth of bone tissues and cells (Figs. 7 and 8).

Moreover, the LaPO$_4$/CS scaffolds exhibited excellent biocompatibility, and the chemical components in the scaffolds were non-toxic. On one hand, BMSCs cultured on the scaffolds proliferated continuously from 1 to 7 days (Fig. 5b); on the other hand, no rejection reaction was observed after implantation of the scaffolds into calvarial bone defect sites (Fig. 9). The above in vitro and in vivo results suggest that LaPO$_4$/CS scaffolds offer great osteoconductivity, cytocompatibility and histocompatibility.

The osteoinductivity of bone scaffolds plays a key role in inducing in vivo new bone formation. To enhance osteogenesis activity, various bioactive elements such as Li, Mg and Sr, are widely incorporated into bone scaffolds [14–16]. For example, Mg^{2+} ions released from implants induce overexpression of calcitonin receptor-like receptor and receptor activity-modifying protein, and thus promote new bone growth [15]. For strontium hydroxyapatite [SrHAP, Ca$_{10-x}$Sr$_x$(PO$_4$)$_6$(OH)$_2$], the synergetic effect between Ca^{2+} and Sr^{2+} ions remarkably increases osteogenic-related gene expression levels and promotes ECM mineralization [16]. La has been reported to penetrates all intercellular spaces and the newly forming bone matrix to enhance the mineral deposition [43], showing its osteoblast potential in tissue engineering. Recent years, La has also been tested to improve proliferation, osteogenic differentiation and mineralization in vitro [44] and stimulates bone formation in a rat model in vivo [45]. In this work, relatively integrated in vivo and in vitro experiments were carried out to obtain a comprehensive understanding of the effects of La^{3+} on the osteogenesis process. Compared with the β-TCP/CS scaffolds, the LaPO$_4$/CS scaffolds presented a better cell proliferation performance (Fig. 5b), indicating positive effects of La on BMSCs. Moreover, the LaPO$_4$/CS scaffolds induced higher ALP activity and ECM mineralization than the β-TCP/CS scaffolds, as demonstrated by the ALP activity assay, ALP staining and alizarin red staining (Figs. 5c and 6), which accelerates new bone formation and mineralization.

To determine the mechanism of LaPO4/CS scaffolds in osteogenesis, RT-PCR analysis and western blotting were employed to measure the expression levels of osteogenic-related genes and proteins. The RT-PCR analysis (Fig. 7a–c) revealed that the expression of ALP, OCN and Col-I were up-regulated by the LaPO$_4$/CS scaffolds. ALP is one of the key enzymes in BMSC differentiation and osteogenesis [46], and higher ALP expression indicates an enhancement of bone formation in vitro. OCN and
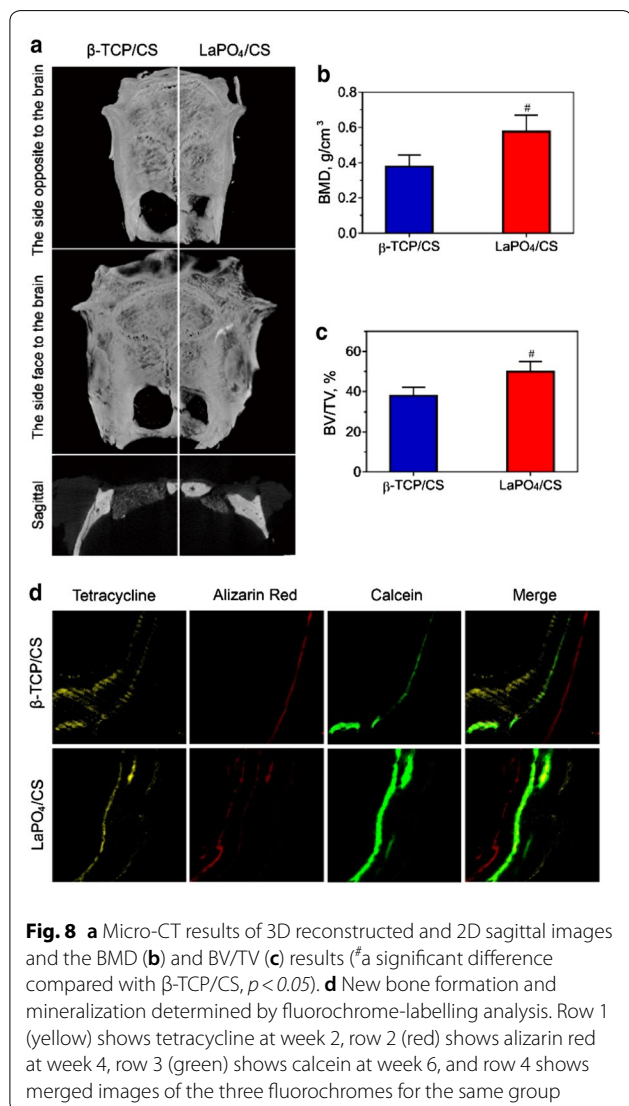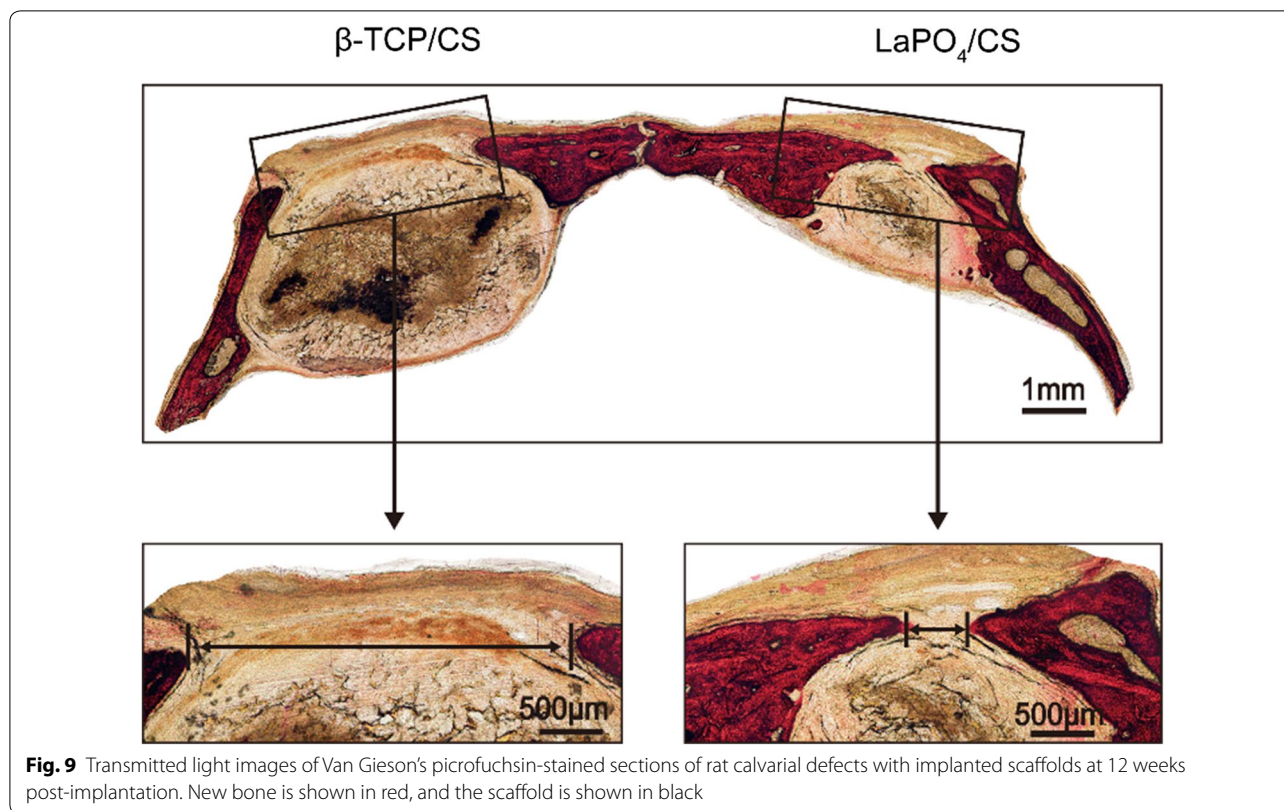
Fig. 9 Transmitted light images of Van Gieson's picrofuchsin-stained sections of rat calvarial defects with implanted scaffolds at 12 weeks post-implantation. New bone is shown in red, and the scaffold is shown in black

Col-I are components of mature bone, and their presence indicates early ECM mineralization. Meanwhile, western blotting was used to assess the cellular signalling processes in BMSCs and verified that LaPO4/CS scaffolds up-regulated the expression of Wnt/β-catenin pathway components (Fig. 7d).

The Wnt/β-catenin pathway is an important pathway that regulates osteogenic differentiation activities [47]. The pathway plays a central role in the bone regeneration and is an important regulator of bone formation in the process of osteoblastic differentiation. It also stimulates its downstream pathways that result in affecting several osteogenic processes including not only osteoblast attachment and differentiation but also cell maturation and apoptosis [48]. Moreover, the pathway has also been reported to promote both mineral deposition in ECM and the repair of tissue defect [49, 50]. The proteins of β-Catenin and Gsk3β are key proteins in the canonical Wnt/β-catenin pathway. The western blotting results suggested that a higher level of GSK3β phosphorylation and increased expression of β-Catenin were induced by LaPO$_4$/CS scaffolds, and this enhancement suggested up-regulation of the Wnt/β-catenin pathway, which would improve cell proliferation and osteogenic differentiation.

In addition, an in vivo study with rat critical-sized calvarial defect sites was conducted to confirm the biofunction of LaPO$_4$/CS scaffolds in bone repair. 3D reconstruction of micro-CT images (Fig. 8a) allowed visualization of the effects of LaPO$_4$/CS scaffolds, and the results were verified by quantitative evaluation of BMD and BV/TV (Fig. 8b, c). Meanwhile, triple fluorochrome and VG staining also showed more bone and collagenous matrix formation at the defect site (Figs. 8d and 9). In summary, LaPO$_4$/CS scaffolds exhibit promising potential for bone regeneration both in vitro and in vivo.

Conclusion

In the present study, LaPO$_4$/CS scaffolds were prepared for bone defect healing. LaPO$_4$ nanoparticles with sizes of 40–60 nm were evenly distributed throughout the surface of the scaffolds. Interconnected 3D macropores were formed due to the connection of the plate-like films, which increased the osteoconductivity of the LaPO$_4$/CS scaffolds for cell adhesion and bone tissue in-growth. The LaPO$_4$/CS scaffolds showed no obvious toxicity or effects on cell morphology, and they accelerated bone generation in a rat cranial defect model. More importantly, controlled release of La^{3+} from the scaffolds was found to promote osteogenic differentiation of BMSCs through the Wnt/β-catenin pathway and enhance the osteogenesis-regulated gene expression of ALP, OCN and Col-I. Furthermore, the LaPO$_4$/CS scaffolds enhanced bone

Hu *et al. J Nanobiotechnol*   (2018) 16:98

Page 12 of 13

regeneration and collagen fibre deposition in rat critical-sized calvarial defect sites. In summary, the novel LaPO$_4$/CS scaffolds provide an admirable and promising platform for the treatment of bone defects.

Additional file

Additional file 1: Figure S1. The hydrodynamic size distribution of LaPO$_4$ agglomerates. **Figure S2.** TG–DTA of samples: (a) LaPO4/CS scaffolds; (b) β-TCP/CS scaffolds. **Figure S3.** XRD patterns of samples: (a) CS powders; (b) β-TCP particles; (c) β-TCP/CS scaffolds. **Figure S4.** FTIR spectra of samples: (a) CS powders; (b) β-TCP particles; (c) β-TCP/CS scaffolds. **Figure S5.** β-TCP/CS scaffold: (a) FESEM images; (b) EDS spectrum. **Figure S6.** In vitro release profile of La$_3$+ ions from LaPO$_4$/CS scaffolds. In vitro release tests of LaPO4/CS scaffolds were carried out after 0.05 g of the samples was soaked in 5 mL deionized water. At different time points, the concentrations of La$_3$+ ions were analysed via inductively coupled plasma/optical emission spectrometry (ICP; iCAP 7000, Thermo Fisher).

Abbreviations

LaPO$_4$: lanthanum phosphate; CS: chitosan; 3D: three dimensional; BMSCs: bone marrow mesenchymal stem cells; Col-I: Collagen I; β-TCP: beta-tricalcium phosphate; HA: hydroxyapatite; BG: bioactive glass; BMP-2: bone morphogenetic protein 2; La: Lanthanum; REEs: rare earth elements; S–D: Sprague–Dawley; RT: room temperature; SEM: scanning electron microscopy; EDS: energy dispersive spectrometry; HRTEM: high resolution transmission electron microscope; SAED: selected area electron diffraction; XRD: X-ray powder diffraction; FTIR: Fourier transform infrared spectroscopy; PBS: phosphate buffer saline; CCK-8: Cell Counting Kit 8; ALP: alkaline phosphatase; pNPP: *p*-nitrophenylphosphate; BCIP/NBT: 5-bromo-4-chloro-3-indolyl phosphate/tetranitroblue tetrazolium chloride; ECM: extracellular matrix; mRNA: messenger RNA; M-MLV: Moloney Murine Leukemia Virus; RT-PCR: reverse transcription-polymerase chain reaction; GAPDH: glyceraldehyde-3-phosphate dehydrogenase; p-GSK3β: phosphorylated glycogen synthase kinase-3β; GSK3: glycogen synthase kinase-3β; micro-CT: micro-computerized tomography; BMD: bone mineral density; BV/TV: bone volume/tissue volume; VG: Van Gieson's; OCN: osteocalcin.

Authors' contributions

HH and PZ carried out experiments, analysed data and wrote the paper. YG, HD and CZ designed the study. JL and QF contributed substantially to the sample preparation. All authors read and approved the final manuscript.

Competing interests

The authors declare that they have no competing interests.

Availability of data and materials

The datasets used and/or analysed during the current study are available from the corresponding author on reasonable request.

Consent for publication

Not applicable.

Ethics approval and consent to participate

All the animal experiments were conducted in accordance with the guidelines and the ethical standards of the Animal Care and Experiment Committee of Shanghai Jiao Tong University Affiliated Sixth People's Hospital.

Publisher's Note

Springer Nature remains neutral with regard to jurisdictional claims in published maps and institutional affiliations.

References

1. Mohammadi M, Alibolandi M, Abnous K, Salmasi Z, Jaafari MR, Ramezani M. Fabrication of hybrid scaffold based on hydroxyapatite-biodegradable nanofibers incorporated with liposomal formulation of BMP-2 peptide for bone tissue engineering. Nanomedicine. 2018;14(7):1987–97.
2. Ahmadzadeh E, Talebnia F, Tabatabaei M, Ahmadzadeh H, Mostaghaci B. Osteoconductive composite graft based on bacterial synthesized hydroxyapatite nanoparticles doped with different ions: from synthesis to in vivo studies. Nanomedicine. 2016;12(5):1387–95.
3. Hu H, Cui R, Mei L, Ni S, Sun H, Zhang C, et al. Cytocompatibility and bone-formation potential of se-coated 316L stainless steel with nano-pit arrays. J Biomed Nanotechnol. 2018;14(4):716–24.
4. Sun D, Chen Y, Tran RT, Xu S, Xie D, Jia C, et al. Citric acid-based hydroxyapatite composite scaffolds enhance calvarial regeneration. Sci Rep. 2014;4:6912.
5. Jang HL, Zheng GB, Park J, Kim HD, Baek HR, Lee HK, et al. In vitro and in vivo evaluation of whitlockite biocompatibility: comparative study with hydroxyapatite and β -tricalcium phosphate. Adv Healthcare Mater. 2016;5(1):128–36.
6. Hails LA, Babister JC, Inglis S, Davis SA, Oreffo RO, Mann S. Inhibition of hydroxyapatite nanoparticle-induced osteogenic activity in skeletal cells by adsorption of serum proteins. Small. 2010;6(18):1986–91.
7. Abu Elella MH, Mohamed RR, Sabaa MW. Synthesis of novel grafted hyaluronic acid with antitumor activity. Carbohydr Polym. 2018;189:107–14.
8. Farokhi M, Mottaghitalab F, Shokrgozar MA, Ou KL, Mao C, Hosseinkhani H. Importance of dual delivery systems for bone tissue engineering. J Control Release. 2016;225:152–69.
9. Quinlan E, Lopez-Noriega A, Thompson E, Kelly HM, Cryan SA, O'Brien FJ. Development of collagen-hydroxyapatite scaffolds incorporating PLGA and alginate microparticles for the controlled delivery of rhBMP-2 for bone tissue engineering. J Control Release. 2015;198:71–9.
10. Chen YX, Zhu R, Ke QF, Gao YS, Zhang CQ, Guo YP. MgAl layered double hydroxide/chitosan porous scaffolds loaded with PFTα to promote bone regeneration. Nanoscale. 2017;9(20):6765.
11. Jiang L, Zhang W, Wei L, Zhou Q, Yang G, Qian N, et al. Early effects of parathyroid hormone on vascularized bone regeneration and implant osseointegration in aged rats. Biomaterials. 2018;179:15–28.
12. Luo Z, Zhang S, Pan J, Shi R, Liu H, Lyu Y, et al. Time-responsive osteogenic niche of stem cells: a sequentially triggered, dual-peptide loaded, alginate hybrid system for promoting cell activity and osteo-differentiation. Biomaterials. 2018;163:25–42.
13. Xavier JR, Thakur T, Desai P, Jaiswal MK, Sears N, Cosgriff-Hernandez E, et al. Bioactive nanoengineered hydrogels for bone tissue engineering: a growth-factor-free approach. ACS Nano. 2015;9(3):3109–18.
14. Clémentlacroix P, Ai M, Morvan F, Romanroman S, Vayssière B, Belleville C, et al. Lrp5-independent activation of Wnt signaling by lithium chloride increases bone formation and bone mass in mice. Proc Natl Acad Sci USA. 2005;102(48):17406–11.
15. Zhao D, Witte F, Lu F, Wang J, Li J, Qin L. Current status on clinical applications of magnesium-based orthopaedic implants: a review from clinical translational perspective. Biomaterials. 2017;112:287–302.
16. Yong L, Xu Z, Ke Q, Yin W, Chen Y, Zhang C, et al. Strontium hydroxyapatite/chitosan nanohybrid scaffolds with enhanced osteoinductivity for bone tissue engineering. Mater Sci Eng. 2017;72:134–42.
17. Zaichick S, Zaichick V, Karandashev V, Nosenko S. Accumulation of rare earth elements in human bone within the lifespan. Metallomics. 2011;3(2):186–94.
18. Manabe R, Fukami K, Ando R, Sakai K, Kusumoto T, Hazama T, et al. Effects of switching from calcium carbonate to lanthanum carbonate

Hu *et al. J Nanobiotechnol*   (2018) 16:98

Page 13 of 13

on bone mineral metabolism in hemodialysis patients. Ther Apher Dial. 2013;17(Supplement S1):35–40.

19. Jiang C, Shang J, Li Z, Qin A, Ouyang Z, Qu X, et al. Lanthanum chloride attenuates osteoclast formation and function via the downregulation of rankl-induced Nf-kappab and Nfatc1 activities. J Cell Physiol. 2016;231(1):142–51.

20. Yang T, Liang Y, Hou J, Dou Y, Zhang W. Metabolizable lanthanum-coordination nanoparticles as efficient radiosensitizers for solid tumor therapy. J Mater Chem. 2017;5(26):5137–44.

21. Chaudan E, Kim J, Tusseau-Nenez S, Goldner P, Malta OL, Peretti J, et al. Polarized luminescence of anisotropic LaPO4: eu nanocrystal polymorphs. J Am Chem Soc. 2018;140(30):9512–7.

22. Runowski M, Dabrowska K, Grzyb T, Miernikiewicz P, Lis S. Core/shell-type nanorods of Tb(3+)-doped LaPO$_4$, modified with amine groups, revealing reduced cytotoxicity. J Nanopart Res. 2013;15:2068.

23. Rojas JV, Woodward JD, Chen N, Rondinone AJ, Castano CH, Mirzadeh S. Synthesis and characterization of lanthanum phosphate nanoparticles as carriers for (223)Ra and (225)Ra for targeted alpha therapy. Nucl Med Biol. 2015;42(7):614–20.

24. Salman AA, Heidelberg T. In situ functionalized fluorescent nanoparticles for efficient receptor coupling. J Nanopart Res. 2014;16(5):1–8.

25. Che D, Zhu X, Liu P, Duan Y, Wang H, Zhang Q, et al. A facile aqueous strategy for the synthesis of high-brightness LaPO 4: eu nanocrystals via controlling the nucleation and growth process. J Lumin. 2014;153(1):369–74.

26. Yang B, Yin J, Chen Y, Pan S, Yao H, Gao Y, et al. 2D-black-phosphorus-reinforced 3D-printed scaffolds: a stepwise countermeasure for osteosarcoma. Adv Mater. 2018;30(10):1705611.

27. Meng Q, Man Z, Dai L, Huang H, Zhang X, Hu X, et al. A composite scaffold of MSC affinity peptide-modified demineralized bone matrix particles and chitosan hydrogel for cartilage regeneration. Sci Rep. 2015;5:17802.

28. Chen J, Pan P, Zhang Y, Zhong S, Zhang Q. Preparation of chitosan/nano hydroxyapatite organic–inorganic hybrid microspheres for bone repair. Colloids Surf. 2015;134:401–7.

29. Enderle R, Gotz-Neunhoeffer F, Gobbels M, Muller FA, Greil P. Influence of magnesium doping on the phase transformation temperature of beta-TCP ceramics examined by Rietveld refinement. Biomaterials. 2005;26(17):3379–84.

30. Frasnelli M, Sglavo VM. Flash sintering of tricalcium phosphate (TCP) bioceramics. J Eur Ceram Soc. 2018;38(1):279–85.

31. Wang X, Zhang L, Zhang Z, Wang X. Effects of pH value on growth morphology of LaPO 4 nanocrystals: investigated from experiment and theoretical calculations. Appl Phys A. 2016;122(5):508.

32. Guo YP, Guan JJ, Chen W, Lei Y, Ke QF, Zhang C. Fabrication of hydroxyapatite/chitosan porous materials for Pb(II) removal from aqueous solution. Rsc Adv. 2015;5(32):25462–70.

33. Yang F, Wen X, Ke QF, Xie XT, Guo YP. pH-responsive mesoporous ZSM-5 zeolites/chitosan core-shell nanodisks loaded with doxorubicin against osteosarcoma. Mater Sci Eng C Mater Biol Appl. 2018;85:142–53.

34. Chen Y, Yu J, Ke Q, Gao Y, Zhang C, Guo Y. Bioinspired fabrication of carbonated hydroxyapatite/chitosan nanohybrid scaffolds loaded with TWS119 for bone regeneration. Chem Eng J. 2018;341:112–25.

35. Rajendran V, Ramamoorthy C. Structural and optical properties of LaPO$_4$ nanostructures by the hydrothermal process and its photocatalytic activity. J Inorg Organomet Polym Mater. 2017;27(6):1886–92.

36. Wang Z, Li JG, Zhu Q, Kim BN, Sun X. Tartrate promoted hydrothermal growth of highly [001] oriented (La 0.95–x Bi x Eu 0.05)PO 4 (x =

0–0.01) nanowires with enhanced photoluminescence. Mater Design. 2017;126:115–22.

37. Kim Y, Yuk H, Zhao R, Chester SA, Zhao X. Printing ferromagnetic domains for untethered fast-transforming soft materials. Nature. 2018;558(7709):274–9.

38. Qi GB, Gao YJ, Wang L, Wang H. Self assembled peptide based nanomaterials for biomedical imaging and therapy. Adv Mater. 2018;30(22):1605021.

39. Dai T, Tanaka M, Huang YY, Hamblin MR. Chitosan preparations for wounds and burns: antimicrobial and wound-healing effects. Expert Rev Anti Infect Ther. 2011;9(7):857–79.

40. Nandi SK, Kundu B, Basu D. Protein growth factors loaded highly porous chitosan scaffold: a comparison of bone healing properties. Mater Sci Eng C Mater Biol Appl. 2013;33(3):1267–75.

41. Venkatesan J, Kim SK. Chitosan composites for bone tissue engineering–an overview. Mar Drugs. 2010;8(8):2252–66.

42. Saravanan S, Leena RS, Selvamurugan N. Chitosan based biocomposite scaffolds for bone tissue engineering. Int J Biol Macromol. 2016;93(Pt B):1354–65.

43. Soares AM, Arana-Chavez VE, Reid AR, Katchburian E. Lanthanum tracer and freeze-fracture studies suggest that compartmentalisation of early bone matrix may be related to initial mineralisation. J Anat. 1992;181(Pt 2):345–56.

44. Liu D, Zhang J, Wang G, Liu X, Wang S, Yang M. The dual-effects of LaCl(3) on the proliferation, osteogenic differentiation, and mineralization of MC3T3-E1 cells. Biol Trace Elem Res. 2012;150(1–3):433–40.

45. Fumoto T, Ito M, Ikeda K. Lanthanum carbonate stimulates bone formation in a rat model of renal insufficiency with low bone turnover. J Bone Miner Metab. 2014;32(5):484–93.

46. Zhang Y, Xia L, Zhai D, Shi M, Luo Y, Feng C, et al. Mesoporous bioactive glass nanolayer-functionalized 3D-printed scaffolds for accelerating osteogenesis and angiogenesis. Nanoscale. 2015;7(45):19207–21.

47. Montes A, Guerrero F, Martinez-Moreno JM, Madueno JA, Herencia C, Peralta A, et al. Magnesium inhibits Wnt/beta-catenin activity and reverses the osteogenic transformation of vascular smooth muscle cells. PLoS ONE. 2014;9(2):e89525.

48. Manolagas SC, Almeida M. Gone with the Wnts: beta-catenin, T-cell factor, forkhead box O, and oxidative stress in age-dependent diseases of bone, lipid, and glucose metabolism. Mol Endocrinol. 2007;21(11):2605–14.

49. Wang W, Zhao L, Ma Q, Wang Q, Chu PK, Zhang Y. The role of the Wnt/beta-catenin pathway in the effect of implant topography on MG63 differentiation. Biomaterials. 2012;33(32):7993–8002.

50. Galli C, Piemontese M, Meikle ST, Santin M, Macaluso GM, Passeri G. Biomimetic coating with phosphoserine-tethered poly(epsilon-lysine) dendrons on titanium surfaces enhances Wnt and osteoblastic differentiation. Clin Oral Implants Res. 2014;25(2):e133–9.